ARTICLE

Dynamically Tunable Multicolor Emissions from Zero-Dimensional Cs_3LnCl_6 (Ln: Europium and Terbium) Nanocrystals with Wide Color Gamut

Received 00th January 20xx,
Accepted 00th January 20xx

DOI: 10.1039/x0xx00000x

Minji Lee,[a,†] Hyesun Chung,[a,†] Seong Vin Hong,[a] Ho Young Woo,[a] Ji-Yeon Chae,[a] Tae Yeol Yoon,[a] Benjamin T. Diroll,[b] Taejong Paik*[a]

This study demonstrates dynamically tunable multicolor emissions from a single component, zero-dimensional (0-D) cesium europium chloride (Cs_3EuCl_6) and cesium terbium chloride (Cs_3TbCl_6) nanocrystals (NCs). Highly uniform colloidal Cs_3EuCl_6 and Cs_3TbCl_6 NCs are synthesized via the heating-up method. Excitation-wavelength-dependent multicolor emissions from Cs_3EuCl_6 and Cs_3TbCl_6 NCs are observed. Under excitation of 330–400 nm, both NCs exhibit blue photoluminescence (PL). Under wavelengths shorter than 330 nm, characteristic red and green emissions are observed from Cs_3EuCl_6 and Cs_3TbCl_6, respectively, owing to the atomic emissions from the f-orbitals in trivalent europium (Eu^{3+}) and terbium (Tb^{3+}) ions. Cs_3EuCl_6 and Cs_3TbCl_6 NCs exhibit broadband excitation spectra and enhanced absorption properties. Particularly, Cs_3EuCl_6 NCs exhibit a very narrow full-width at half-maximum in both blue and red PL and no overlap between the two spectra. The photophysical properties of these NCs are further investigated to understand the multicolor PL origins by time-resolved and temperature-dependent PL measurements. Finally, the potential applications of Cs_3EuCl_6 and Cs_3TbCl_6 NCs as anti-counterfeiting inks for high-level security are demonstrated. Given their broadband excitation with enhanced absorption properties and dynamically tunable colors with a wide color gamut, Cs_3EuCl_6 and Cs_3TbCl_6 NCs have great potential as novel multicolor NC emitters for many emerging applications.

Introduction

Multicolor-emitting nanocrystals (NCs) have attracted significant attention for many emerging applications. Generally, luminescent NCs afford a single emission color that is determined during the synthetic procedure, which is tailored by changing the size,[1, 2] shape,[3-5] and composition of NCs[6, 7] or by incorporating dopants.[8, 9] In contrast, luminescent colors of multicolor-emitting NCs are tailored via external stimuli such as pressure,[10] temperature,[11, 12] and excitation power.[13, 14] Particularly, multicolor luminescence that is tailored using the excitation wavelength enables the facile and reversible change of luminescence colors from a single NC.[15, 16] Multicolor-emitting NCs potentially provide complex optical information using multimode encryption, enabling a high level of security and anti-counterfeit protection.[17-20] Moreover, multicolor-emitting NCs can also be utilized for optical thermometry[21] and as bioimaging agents with enhanced sensitivity and resolution.[22, 23]

To date, excitation-wavelength-dependent multicolor emissions from colloidal NCs have been demonstrated using carbon-based NCs[24-26] and semiconducting NCs.[27] However, these NCs suffer from drawbacks such as large spectral overlap between multiple emission spectra, small change of the emission wavelength, and broad emission bandwidth. Recently, zero-dimensional (0-D) ternary metal halide NCs have attracted significant attention as a promising platform for highly efficient multicolor-emitting NCs. 0-D metal halide, comprising completely isolated metal halide octahedra ($[ML_6]^{3-}$) in the crystal structures, exhibit high luminescence properties owing to the enhanced radiative recombination of excitons from isolated $[ML_6]^{3-}$.[28-30] When multiple metal ions among Bi,[31] Sn,[32] In,[33] Mn,[34] and Pb[32] are incorporated in 0-D metal halide structures, each metal ion can act as an emission center in the isolated 0-D octahedra units, resulting in multiple photoluminescence (PL) lines from a single component, which are tailored by the excitation wavelength. However, NC-based luminescent metal halide, which exhibit tunable multicolor emission over a wide color gamut and small spectral overlap in a single component, have rarely been reported in literature thus far.

Among the various types of metal halide NCs, lanthanide-based metal halide NCs exhibit characteristic luminescence and multifunctional properties owing to the presence of the f-block lanthanide elements.[35-38] Lanthanide elements have partially filled 4f shells, which are responsible for their characteristic optical and magnetic properties.[39, 40] The sharp atomic transition between f-orbitals enables the characteristic absorption and emission bands depending on the type of lanthanide elements.[41] Additionally, electronic transitions between f-orbitals are parity forbidden, resulting in a long excited state lifetimes, typically from micro- to millisecond scale, which enables the multiphoton upconversion (UC) and downconversion (DC) processes.[42] Dynamically tunable multicolor emissions from lanthanide-based NCs have also been demonstrated in UC NCs. For example, multicolor emission can

be produced from core-shell UC NCs by adjusting the pulse width of infrared laser beams[43] or by manipulating the luminescence decay lifetimes.[44] However, owing to the parity forbidden transition between f-orbitals and narrow absorption bandwidth, low molar extinction coefficients require high-energy infrared laser excitation, which limits the application versatility of multicolor UC NCs.

Here, excitation-wavelength-dependent multicolor emissions are demonstrated from a single component from 0-D cesium europium chloride and terbium chloride (Cs_3EuCl_6 and Cs_3TbCl_6, respectively) NCs under broadband ultraviolet (UV) excitation and with a wide color gamut. 0-D Cs_3EuCl_6 or Cs_3TbCl_6 NCs were synthesized via heating-up synthesis using cesium chloride and lanthanide chloride precursors. Blue PL was observed under excitation of 330–400 nm from both NCs. For wavelength excitation of less than 330 nm, characteristic red or green emissions were observed due to the atomic emissions from the f-orbitals in trivalent europium (Eu^{3+}) and terbium (Tb^{3+}) ions. Cs_3EuCl_6 and Cs_3TbCl_6 NCs exhibited broadband excitation spectra and enhanced absorption compared to the f–f transition in lanthanide ions. This signifies that the atomic emissions from Eu^{3+} and Tb^{3+} ions are attributed to the charge transfer from metal–halide complexes in NCs, not from a direct excitation of f–states. The PL properties of Cs_3EuCl_6 and Cs_3TbCl_6 NCs are dynamically tunable by changing the excitation wavelength. A wide range of PL change was observed between blue and red colors in Cs_3EuCl_6 and blue and green colors in Cs_3TbCl_6 NCs. Particularly, Cs_3EuCl_6 NCs exhibited a very narrow full-width at half-maximum (FWHM) in both blue and red PL, with no overlap between the two PL spectra. Furthermore, the photophysical properties of Cs_3EuCl_6 and Cs_3TbCl_6 NCs were analyzed to understand the luminescent mechanism of multicolor PL. Finally, the potential application of Cs_3EuCl_6 and Cs_3TbCl_6 NCs in anti-counterfeit security was demonstrated. Given their broadband excitation with enhanced absorption properties and dynamically tunable colors with a wide color gamut from a single NC, these NCs offer great potential as novel multicolor NC emitters for anti-counterfeiting inks.

Results and Discussion

Colloidal Cs_3EuCl_6 and Cs_3TbCl_6 NCs were synthesized by the previously reported heating-up method.[35, 45] The reaction was performed at 260 °C for 1 h. The reaction solution was transparent yellow before heating and turned opaque brown with europium and opaque white with terbium during the reaction, indicating the formation of NCs. As-synthesized NCs exhibit high colloidal stability in nonpolar solvents. Figure 1 displays the Transmission electron microscopy (TEM) images of Cs_3EuCl_6 and Cs_3TbCl_6 NCs. Highly uniform NCs were synthesized with sizes of 19.51 ± 1.72 nm for Cs_3EuCl_6 NCs and 14.96 ± 1.43 nm for Cs_3TbCl_6 NCs, which were determined via the statistical analysis of more than 180 NCs from the TEM images (Figures S1 and S2). The energy dispersive x-ray (EDX) images exhibit the homogeneous distribution of cesium, europium or terbium, and chlorine atoms in the Cs_3EuCl_6 and Cs_3TbCl_6 NCs (Figures S3 and S4).

Figure 2a shows the powder X-ray diffraction (XRD) patterns of Cs_3EuCl_6 and Cs_3TbCl_6 NCs and their simulated patterns constructed from the crystallographic data reported in literature (Tables S1 and S2).[46, 47] The XRD results reveal that the Cs_3EuCl_6 and Cs_3TbCl_6 NCs are in monoclinic phase with a *C2/c* space group (#15). No impurities or remaining CsCl peaks are observed in the XRD patterns. The high-resolution TEM (HR-

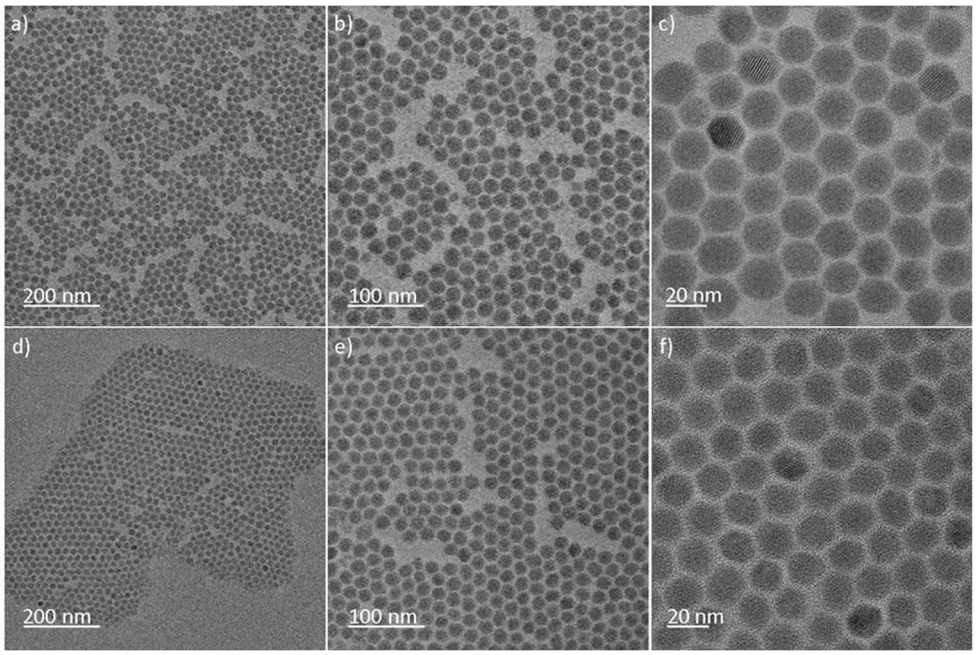

Fig. 1 Low-magnification and high-magnification TEM images of a–c) Cs_3EuCl_6 NCs and d–f) Cs_3TbCl_6 NCs.

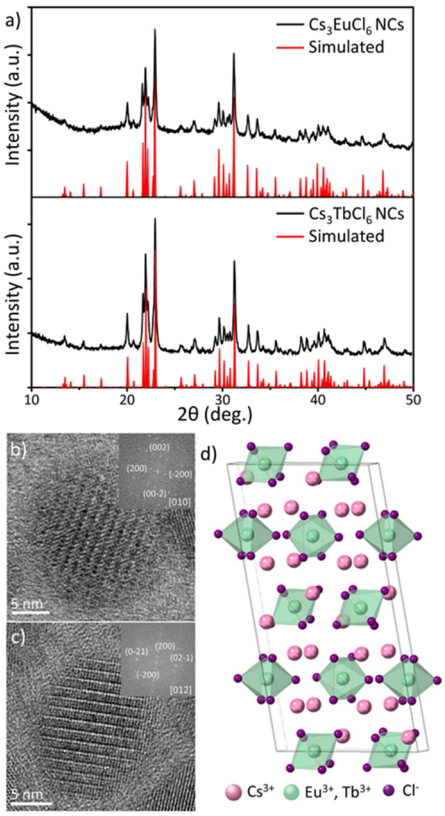

Fig. 2 XRD patterns of a) Cs_3EuCl_6 and Cs_3TbCl_6 NCs, and their simulated XRD patterns constructed using structural parameters obtained from references 36 and 37 (red lines). HR-TEM and FFT images of a single b) Cs_3EuCl_6 and c) Cs_3TbCl_6 NC. d) Schematic of the atomic unit cell of the monoclinic phase $Cs_3(Eu,Tb)Cl_6$ structure.

TEM) image displays crystalline lattice fringes of Cs_3EuCl_6 NCs (Figures 2b and 2c). Single crystal patterns are observed in the fast Fourier transformation (FFT) patterns of the HR-TEM images, which is consistent with the simulated electron diffraction (ED) patterns from the monoclinic phase structural parameters (Figures 2a and 2b inset and S5). Figure 2d exhibits a schematic of the monoclinic crystal structure of Cs_3EuCl_6 and Cs_3TbCl_6 NCs. Trivalent lanthanide cations (Eu^{3+} or Tb^{3+}) are located at the center of the metal halide octahedra. For Cs_3EuCl_6, the central Eu^{3+} ions are separated by a distance of 7.3 Å, which is much longer than the double of Eu–Cl bond lengths (5.97 Å, Figure S6). Additionally, the Cl distance between the nearest neighbor octahedra is longer than the covalent bonding distance between Cl_2 molecules, revealing that $[EuCl_6]^{3-}$ octahedra are completely separated by cesium cations (Cs^+) in the crystal structure and form the 0-D metal halide structure.

0-D Cs_3EuCl_6 and Cs_3TbCl_6 NCs exhibit multicolor PL properties, which can be dynamically tuned by changing the excitation wavelength. Figures 3a and 3b exhibit the room-temperature PL and PL excitation (PLE) spectra of Cs_3EuCl_6 NCs. Under the excitation of 280 nm, characteristic red luminescence is observed owing to the f–f transition of Eu^{3+} ions in the Cs_3EuCl_6 NCs. Sharp atomic emission peaks are observed at 590, 611, 652, and 700 nm, which is attributed to the radiative transition from ^5D_o levels to $^8S_{7/2j}$ (J = 1–4) levels in Eu^{3+} ions. On the other hand, when Cs_3EuCl_6 NCs are excited at 350 nm, a deep-blue PL is observed at 430 nm of the PL maxima and with small intensities of red emission at 590 and 611 nm, which are attributed to the Eu^{3+} Ions. A highly symmetric and narrow PL peak is observed with a FWHM of 26.11 nm and a large Stokes shift of 117 nm between PL and PLE maximum None of the f–f excitonic peaks in Eu^{3+} ions exist in this wavelength range, indicating that the intense blue PL does not stem from the f-states of Eu^{3+} ions. Blue PL of 0D Cs_3LnCl_6 (Ln: lanthanide) NCs under UV excitation have been previously reported by our group.[35] The 0D host emission from Cs_3LnCl_6 NCs exhibit a broadband, asymmetric emission profile. In contrast, Cs_3EuCl_6 NCs exhibit highly symmetric and very narrow PL spectra, which is inconsistent with the PL characteristic of 0D Cs_3LnCl_6 NCs. The PL peak position and relatively symmetric narrow linewidth indicate that the 430 nm PL may be attributed to the $4f^7$–$4f^65d^1$ transition from divalent europium (Eu^{2+}) ions, as reported for $CsEuCl_3$ and Eu^{2+}-doped CsBr NCs.[48-50] However, the possibility of blue PL, which is attributed to the 0D structure of Cs_3EuCl_6 NCs may not be completely excluded. The X-ray photoemission spectra (XPS) of Cs_3EuCl_6 NCs confirm a mixed valence state of

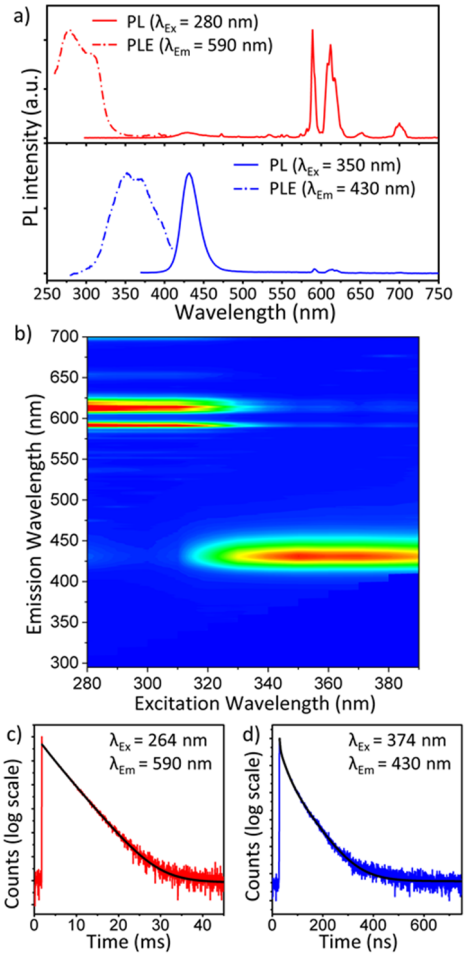

Fig. 3 a) PL spectra of Cs_3EuCl_6 NCs excited at 350 nm (blue line) and 280 nm (red line) and PLE spectra monitored at 611 nm (red dashed line) and 430 nm (blue dashed line). b) 2-D PL spectra with varying excitation wavelengths from 280 nm to 390 nm with a 10 nm interval. TRPL curves of Cs_3EuCl_6 NCs monitored at c) 590 nm (λ_{ex} = 264 nm) and d) 430 nm (λ_{ex} = 374 nm).

$Eu^{2+}/(Eu^{2+}+Eu^{3+})$ with 39.5% of atomic percentage, indicating the presence of Eu^{2+} owing to the partial reduction during the synthesis (Figure S7). Time-resolved photoluminescence (TRPL) decay lifetimes also display the different origins from blue and red PL. TRPL profiles of the Cs_3EuCl_6 NCs were monitored at 590 and 430 nm under 264 and 374 nm excitation, respectively (Figures 3c, 3d and Table S3). The emission decay lifetime at 590 nm was measured to be 3.99 ms with single exponential characteristic. This long decay lifetime clearly indicates that the red PL is attributed to the forbidden f–f transition in Eu^{3+} ions. On the other hand, the decay lifetime under excitation of 374 nm shows multiexponential decay with average lifetime of 25.79 ns. The radiative decay profile reported in Eu^{2+} occupied in single site of hosts exhibits single exponential behaviour. With increasing content of Eu^{2+} ions, decay profile is deviated from a single exponential function and decay lifetime becomes faster owing to the Eu^{2+}-Eu^{2+} interaction.[51] Multiexponential decay profile of Cs_3EuCl_6 NCs with reduced lifetime compared to reported Eu^{2+}-phosphors may be attributed to high concentration of Eu^{2+} in a single NC. Characteristic PL decay profiles depending on high and low energy excitation clearly indicate that the multicolor PL of Cs_3EuCl_6 NCs originates via different emission mechanisms within a single NC. The schematic of the energy diagram of Cs_3EuCl_6 NCs depending on the excitation wavelength was displayed in Figure S8.

The weak absorption cross-section and very narrow absorption bandwidth of the f–f transition are a major limitation of lanthanide-based luminescence materials.[42] Thus, numerous studies have been conducted to design broadband sensitization of trivalent lanthanide ions to overcome these drawbacks.[52-54] Our Cs_3EuCl_6 NCs afford a broadband and efficient sensitization for f-electrons in Eu^{3+} ions and blue PL, providing great potential for highly efficient novel lanthanide-based emitters. PLE spectra were monitored at 611 nm of the $^5D_0$ –> $^7F_2$ transition of Eu^{3+} ions. The broadband PLE spectrum was observed in the range of 250–330 nm, which is denoted as excitation band 1. This PLE spectrum is distinct from sharp atomic absorption owing to the f–f transition in Eu^{3+} ions and may stem from the charge transfer transition from NC hosts to Eu^{3+} (e.g., Cl^- -> Eu^{3+}).[55] The f–f absorption peaks of Eu^{3+} ions, such as $^7F_0$ to $^5H_6$, $^5D_4$, $^5L_7$, and $^5L_6$ transitions, were not clearly visible in the PLE spectra, representing the intense absorption of excitation band 1 compared to the forbidden f–f transition in Eu^{3+} ions. Additionally, the PLE spectra for blue PL spanned from 300 to 420 nm, which is denoted as excitation band 2. The PLE spectra of excitation bands 1 and 2 were consistent with the absorption of Cs_3EuCl_6 NCs. The Tauc plot of Cs_3EuCl_6 NCs displays an absorption onset at 417 nm (2.97 eV), which is consistent with the absorption bands of the $4f^7$–$4f^65d^1$ transition in Eu^{2+} for blue PL (Figure S9). A second absorption peak appears at approximately 342 nm (3.62 eV) of onset wavelength, corresponding to the high energy excitation for f-emissions in Eu^{3+}. Absolute PL quantum yields (PLQYs) of Cs_3EuCl_6 NCs measured with the integrating sphere were 48.78% for red PL and 5.38% for blue PL. The results of PL, PLE, PLQY, and lifetime of Cs_3EuCl_6 NCs under high and low energy excitation are tabulated in Table S4. Moreover, large Stokes shifts of 212 nm for red PL and 117 nm for blue PL were observed, which reduces self-absorption.

To further understand the luminescence properties, low-temperature PL measurements were performed from 300 K to 80 K under 280 nm and 350 nm excitation (Figure S10). For both excitation wavelength, the intensity of blue and red PL increased with decreasing temperature. This is attributed to the decrease of the thermal quenching with decreasing temperature, which resulted in enhanced radiative recombination. Eu^{2+} and Eu^{3+} behave as independent emission centers without any significant PL changes due to the energy or charge transfer between the two centers. Thermal quenching from Eu^{2+} is described by the thermally activated nonradiative relaxation by cross-over from the excited 5d state to the ground 4f state or the thermal ionization of the 5d electron to conduction band in the host lattice.[56, 57] The thermal quenching behavior is described by the Eq. (1)

$$I(T) = \frac{I_0}{1+Ae^{(-Ea/k_BT)}} \quad (1)$$

where T is the absolute temperature, k_B is the Boltzmann constant, E_a is the activation energy for thermal quenching, and I(T) and I_0 are the integrated PL intensity at temperature T and estimated integrated PL at T= 0K, respectively. Figure S11 displays the integrated PL intensity versus 1000/T graph. The activation energy E_a for thermal quenching, which is calculated by fitting with Eq (1), is 0.124 eV. This value is similar to the E_a of Eu^{2+} phosphors[58, 59] but slightly smaller than E_a of 0D metal halides.[29, 60] The narrow FWHM and low E_a values of Cs_3EuCl_6 NCs compared to those of the 0D metal halides signifies that the blue PL from Cs_3EuCl_6 NCs may be attributed to the emission from Eu^{2+} centers. The temperature-dependent Eu^{3+} emission under 280 nm excitation also exhibited an increase of the integrated PL with decreasing T. The activation energy was calculated to be 76.6 meV, which is smaller than those of the Eu^{3+}-doped phosphors reported in literature.[61] The E_a for Eu^{3+} emission is influenced by several factors, such as the host structure[56, 62] and doping concentration of Eu^{3+} ions.[63] The high Eu^{3+} concentration in our Cs_3EuCl_6 NCs may facilitate thermally activated concentration quenching between Eu^{3+} emission centers, resulting in small E_a for thermal quenching.

We further investigated the tunable multicolor PL properties using Cs_3TbCl_6 NCs. Figure 4a and 4b display the PL and PLE spectra of Cs_3TbCl_6 NCs. Under high-energy excitation (band 1), characteristic green PL was observed at 490, 548, 583, and 621 nm, which is assigned as the ^5D_o -> ^7D_J (J = 6–3) transition in the f-orbitals of trivalent Tb^{3+} ions, as displayed in Figure S12. On te other hand, under broad band excitation from 300 to 410 nm (band 2), blue PL was observed at 430 nm PL maxima, which is similar to the PLE properties of the 0D Cs_3LnCl_6 NCs.[35] However, the characteristic green atomic emissions from f-orbitals in Tb^{3+} ions coexisted. Low-temperature PL measurements showed that both blue and green PL intensity of Cs_3TbCl_6 NCs continuously increased with decreasing temperatures (Figure S13), revealing the reduction of non-radiative thermal quenching at low temperature. This may indicate that energy or

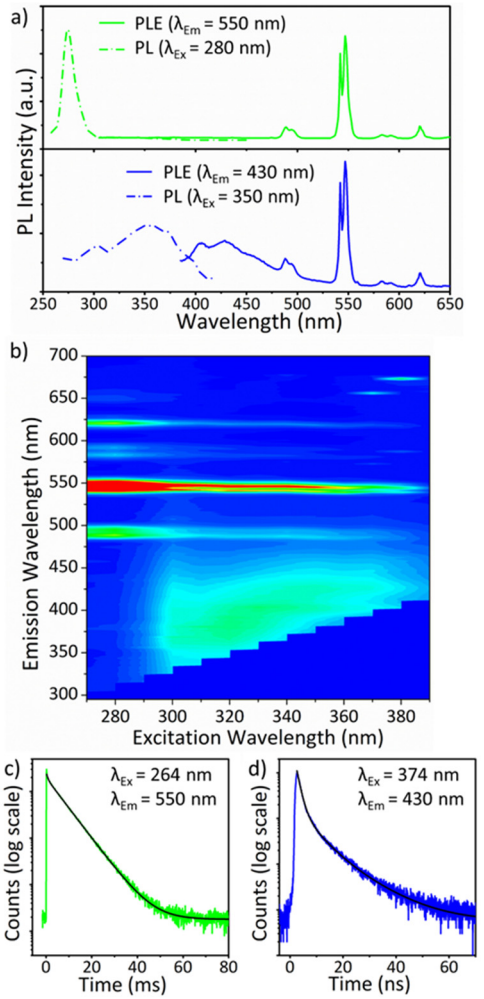

Fig. 4 a) PL spectra of Cs_3TbCl_6 NCs excited at 280 nm (green line) and 350 nm (blue line) and PLE spectra monitored at 550 nm (green dashed line) and 430 nm (blue dashed line). d) PL spectra with varying excitation wavelengths from 270 to 390 nm with a 10 nm interval. TRPL curves of Cs_3TbCl_6 NCs monitored at c) 550 nm (λ_{ex} = 264 nm) and d) 430 nm (λ_{ex} = 374 nm).

charge transfer between NC hosts and Tb^{3+} states did not significantly affect the PL process. The Tauc plot of Cs_3TbCl_6 NCs shows the weak absorption at an onset wavelength of 413 nm (3.00 eV), corresponding to the onset wavelength of the PLE spectrum for the blue PL. Additionally, strong absorption in the short wavelength region was observed at the onset wavelength of 298 nm (4.15 eV), corresponding to the onset wavelength of the PLE spectrum for the green PL (Figure S14). Similar to the Cs_3EuCl_6 NCs, a long PL lifetime of 5.53 ms was observed for green PL at 550 nm under excitation of 264 nm, which is attributed to the f–f forbidden transition in Tb^{3+} ions (Figures 4c, 4d and Table S5). On the other hand, the radiative decay lifetime of blue PL was fitted a multieponential function with average decay lifetime of 2.16 ns. The decay pathway is be attributed to carrier trap, charge recombination, and the trap-state-associated decay.[64] PLQYs of Cs_3TbCl_6 NCs were 36.85% for green PL and 6.49% for blue PL. The results of PL, PLE, PLQY, and lifetime of Cs_3TbCl_6 NCs under high and low energy excitation are tabulated in Table S6.

Since PL from excitation bands 1 and 2 of Cs_3EuCl_6 and Cs_3TbCl_6 NCs are largely separated with a small portion of spectral overlap (Figure S15), the PL colors of these NCs can be systematically tuned by changing the excitation wavelengths. Figure 5a displays photographs of the excitation-wavelength-dependent PL colors of the Cs_3EuCl_6 and Cs_3TbCl_6 NC films. As discussed earlier, the excitation dependent emission is attributed to the presence of two different emission mechanisms in a single NC. For examples, Cs_3EuCl_6 NCs have 4f7–4f65d1 emission from Eu^{2+} for blue PL and f-f transition from Eu^{3+} for red PL depending on the excitation wavelength. Cs_3EuCl_6 NCs exhibits red PL under the excitation range from 260 to 330 nm and blue PL under the excitation range of 310 nm to 360 nm. Therefore, the PLE spectra of blue and red PL are partially overlapped in the range between 310 nm and 330 nm. In this range, the relative PL intensity ratio of blue and red PL can be systematically varied by change of the excitation wavelength, which enables fine tuning of emission color over wide spectrum range between blue and red, as described in Figure 5a. As the excitation wavelength is shifted to wavelengths longer than 310 nm, the emission color of Cs_3EuCl_6 NCs is tuned to purple owing to the mixed emissions from both Eu^{2+} and Eu^{3+} ions, and subsequently, it turns blue owing to the pure Eu^{2+} PL. In the same way, Cs_3TbCl_6 NCs have blue emission from NC hosts and green emission from f-f transition of Tb^{3+} ions. Depending on the excitation wavelength, Cs_3TbCl_6 NCs exhibited the blue or green emission solely, or the mixed emission profile of blue and green when the excitation wavelength is selected in the range of PLE overlap between blue and green PL. Therefore, green PL is observed at high-energy excitation larger than 310 nm, and the emission color turns greenish blue as the excitation wavelength increases. Figure 5b displays the 1931 Commission Internationale de L'Eclairage (CIE) color space of the PL spectra of Cs_3EuCl_6 and Cs_3TbCl_6 NCs under excitations from 280 to 380 nm. The CIE color coordinates of the red and blue emissions from the Cs_3EuCl_6 NCs are (0.56, 0.33) and (0.17, 0.04), respectively, which are close to the CIE of standard red and blue ((0.64, 0.33) and (0.15, 0.06)) of sRGB/Rec.709 standard color gamut. Additionally, the CIE color coordinate of the green emission from the Cs_3TbCl_6 NCs is (0.30, 0.66), which fits perfectly with the sRGB/Rec.709 standard green (0.30, 0.60). The tunable PL emission covers 88.6% of Rec. 709, 65.5% of NTSC 1987, and 49.6% of Rec. 2020 color space, representing a wide color gamut of tunable colors.

Dynamic color changes under conventional UV light makes our Cs_3EuCl_6 and Cs_3TbCl_6 NCs potential writeable and printable security inks for high-level anti-counterfeiting. Figure 5c shows the direct writing of a flower image on a printing paper using Cs_3EuCl_6 and Cs_3TbCl_6 NCs and a writing brush. The marked image was invisible under ambient light; thus, the images can be effectively hidden. Under 365 nm irradiation, a blue flower image emerges owing to the luminescence from both the NC hosts. The luminescent color of this image changed to red and green under 254 nm excitation owing to the PL of the Eu^{3+} and Tb^{3+} ions, respectively. Notably, this multicolor image was clearly visible under the UV irradiation using a conventional hand UV and not using a high-power laser or time-gating

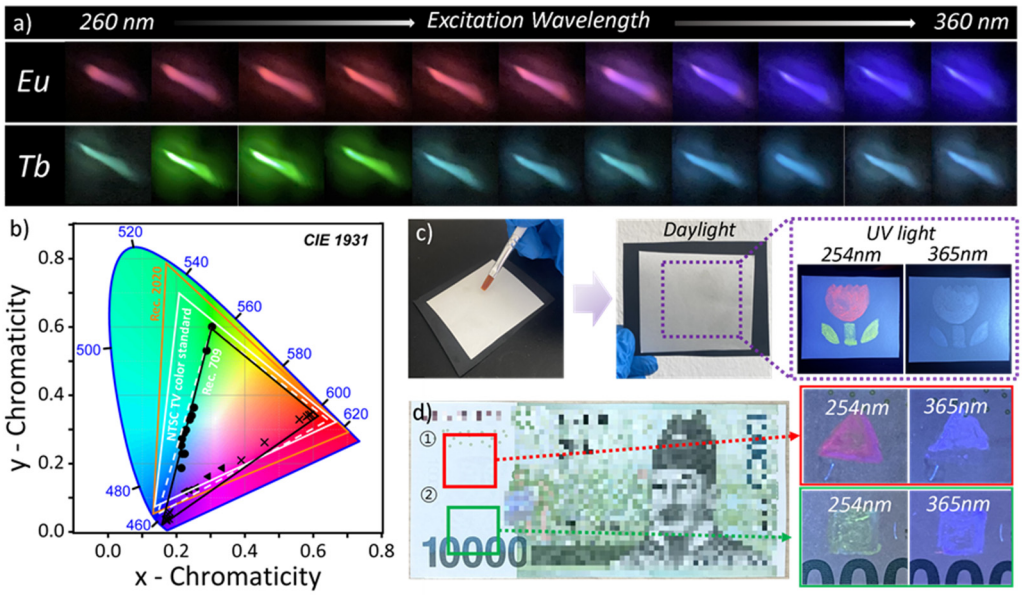

Fig. 5 Photographs of PL of a) Cs_3EuCl_6 and Cs_3TbCl_6 NC films under excitation wavelengths from 260 to 360 nm with a 10 nm interval. b) CIE coordinates of Cs_3EuCl_6 (X points) and Cs_3TbCl_6 (● points) NCs under excitations from 280 to 380 nm in 10 nm increments. Additional ▲ points represent CIE coordinates of Cs_3EuCl_6 NCs under excitations from 322 to 330 nm in 2 nm increments. Photographs of anti-counterfeiting marks formed by c) direct writing using a brush and d) transfer printing under ambient light, a 254 nm UV light, and a 365 nm UV light.

equipment. We believe that much higher-level security of anti-counterfeiting can be achieved using fluorescence lifetime imaging owing to the large difference in the PL lifetime between NC hosts and Ln^{3+} ions. Moreover, the transfer printing of security marks using a NC solution and rubber stamps is demonstrated. For transfer printing, UV plasma treatment was performed on the surface of the rubber stamp, and then, the NC solution was drop-casted on the stamp followed by vacuum drying. The stamps were pressed on the desired substrates to transfer the NC films. Figure 5d displays the stamped NC films on a currency note under ambient light and UV irradiation. The stamped images clearly show blue/red (Eu) or blue/green (Tb) dual-mode PL depending on the excitation wavelength. The NC marks were easily transferred regardless of the type of substrates, as described in Figure S16 which shows the potential of applying our Cs_3EuCl_6 and Cs_3TbCl_6 NCs in broad anti-counterfeiting fields.

Conclusions

In summary, this study reported the dynamically tunable multicolor emission of Cs_3EuCl_6 and Cs_3TbCl_6 NCs with a wide color gamut. Colloidal synthesis of Cs_3EuCl_6 and Cs_3TbCl_6 NCs was performed via the heating-up process using CsCl and $LnCl_3$ precursors in the presence of OA, OM, and ODE solvents. Monoclinic-phase, 0-D Cs_3EuCl_6 and Cs_3TbCl_6 NCs were synthesized with high size uniformity and phase purity. The as-synthesized NCs exhibited excitation-wavelength-dependent multicolor emission with broadband absorption properties and large Stokes shifts. The multicolor PL from 0-D Cs_3EuCl_6 and Cs_3TbCl_6 NCs stemmed from different emission mechanisms in a single NC. TRPL and low-temperature PL measurements revealed that Cs_3EuCl_6 NCs exhibited red PL under 254 nm excitation and blue PL under 365 nm excitation, which is attributed to the f–f transition in Eu^{3+} ions and $4f^7$–$4f^65d^1$ transition in Eu^{2+} ions, respectively. Furthermore, Cs_3TbCl_6 NCs exhibited green PL under 254 nm excitation and blue PL under 365 nm excitation, corresponding to the PL from f-states of Tb^{3+} and from 0-D NC hosts. The tunable PL from 0-D Cs_3EuCl_6 and Cs_3TbCl_6 NCs covered a wide color gamut with 88.6% of Rec.709, 65.5% of NTSC 1987, and 49.6% of Rec.2020. Finally, the potential application of 0-D Cs_3EuCl_6 and Cs_3TbCl_6 NCs in anti-counterfeiting inks was demonstrated. Multicolor NC marks were deposited via direct writing using a brush or transfer printing on various substrates. These marks were invisible in ambient light but provided different color codes depending on the excitation wavelength (254 and 365 nm). Given their broadband excitation, enhanced absorption, and tunable PL properties with a wide color gamut, 0-D Cs_3EuCl_6 and Cs_3TbCl_6 NCs exhibit great potential in multilevel anti-counterfeiting applications.

Materials and Methods

Chemicals

Cesium chloride (CsCl, reagent plus, trace metals basis, 99.9%, Sigma Aldrich), europium(III) chloride ($EuCl_3$, 99.99% trace metals basis, Sigma Aldrich), terbium(III) chloride hexahydrate ($TbCl_3{\cdot}6H_2O$, 99.9%, Alfa Aesar), 1-octadecene (ODE) (90%, Sigma Aldrich), oleic acid (OA) (90%, Sigma Aldrich), and oleylamine (OM) (70%, Sigma Aldrich) were used as received.

Synthesis of Cs_3EuCl_6 NCs

CsCl (4.48 mmol) and $EuCl_3$ (1.12 mmol) were added to a 100-mL three-neck flask along with 20 mL of ODE, 1.5 mL of OA, and 1.5 mL of OM. The mixture was heated at 120 ℃ under vacuum for 2 h. Subsequently, the mixture was heated at 260 ℃ under

N_2 atmosphere for 45 min. The solution was then cooled to 25–40 °C and diluted with anhydrous toluene. Cs_3EuCl_6 NCs remained dissolved in the solvent, whereas the unreacted CsCl precursors precipitated. The supernatant solution comprising the Cs_3EuCl_6 NCs was separated from the CsCl precipitate and centrifuged at 8000 rpm for 2 min to precipitate the Cs_3EuCl_6 NCs. Then, Cs_3EuCl_6 NCs were redispersed in anhydrous toluene and stored in a glovebox.

Synthesis of Cs_3TbCl_6 NCs

Cs_3TbCl_6 NCs were prepared following a procedure similar to that used for synthesizing Cs_3EuCl_6 NCs using 1.12 mmol of the $TbCl_3{\cdot}6H_2O$ precursors. To synthesize Cs_3TbCl_6 NCs, the reactions were performed at 260 ℃ for 50 min.

Characterization

TEM, HR-TEM, scanning TEM (STEM), and EDX spectroscopy images were collected using a JEOL JEM-F200 system operating at 200 kV. The diffuse reflectance spectra were collected using a JASCO V-770 spectrometer. PL spectra were obtained using an Edinburgh FS5. PLQYs were measured using a fluorimeter equipped with an integrating sphere. Before the PLQY measurements, coumarin 1 dispersed in ethanol (PLQY of 73%) was measured for comparison and calibration. Time-resolved photoluminescence (TRPL) decay data were collected using a HORIBA Fluorolog-3 with a single photon-counting photomultiplier tube under a 374 nm pulsed laser diode. Low-temperature PL spectra were obtained using an Edinburgh FS5 with Oxford Instruments Optistat DN-X 77K nitrogen bath. XRD was performed using a Bruker-AXS New D8-Advance diffractometer using a Cu Kα1 radiation source. Simulated XRD patterns were constructed with CrystalDiffract6 Software, using the structure factor FHKL with the reported crystal structure.[46, 47] The structure factor is derived by summing the amplitude scattered by each atom in the unit cell as follows:

$$F(hkl) = \sum_{n=1}^{N} f_n \exp\{2\pi i(hx_n + ky_n + lz_n)\}$$

where hkl are the Miller indices of reflection, f_n is the atomic scattering factor of the nth atom in the unit cell, and $\{x_n, y_n, z_n\}$ are the fractional coordinates of the atoms.

Author Contributions

Conflicts of interest

There are no conflicts to declare.

Acknowledgements

M. Lee and H. Chung contributed equally to this work. This research was supported by the Creative Materials Discovery Program through the National Research Foundation of Korea (NRF) funded by the Ministry of Science and ICT (MSIT) (NRF-2018M3D1A1059001) and NRF grants 2022R1A4A2000776, 2021M3H4A3A01062960, and 2021R1A2C1013604. Work performed at the Center for Nanoscale Materials, a U.S. Department of Energy Office of Science User Facility, was supported by the U.S. DOE, Office of Basic Energy Sciences, under Contract No. DE-AC02-06CH11357.

References

1 R. Xie, D. Battaglia and X. Peng, *J. Am. Chem. Soc.*, 2007, **129**, 15432-15433.
2 C. B. Murray, D. J. Norris and M. G. Bawendi, *J. Am. Chem. Soc.*, 1993, **115**, 8706-8715.
3 L. Carbone, C. Nobile, M. D. Giorgi, F. D. Sala, G. Morello, P. Pompa, M. Hytch, E. Snoeck, A. Fiore, I. R. Franchini, M. Nadasan, A. F. Silvestre, L. Chiodo, S. Kudera, R. Cingolani, R. Krahne and L. Manna, *Nano Lett.*, 2007, **7**, 2942-2950.
4 A. C. Bartnik, A. L. Efros, W.-K. Koh, C. B. Murray and F. W. Wise, *Phys. Rev. B*, 2010, **82**, 195313.
5 J. Kwon, W. J. Choi, U. Jeong, W. Jung, I. Hwang, K. H. Park, S. G. Ko, S. M. Park, N. A. Kotov and J. Yeom, *Nano Converg.*, 2022, **9**, 32.
6 G. Nedelcu, L. Protesescu, S. Yakunin, M. I. Bodnarchuk, M. J. Grotevent and M. V. Kovalenko, *Nano Lett.*, 2015, **15**, 5635-5640.
7 C. Coughlan, M. Ibáñez, O. Dobrozhan, A. Singh, A. Cabot and K. M. Ryan, *Chem. Rev.*, 2017, **117**, 5865-6109.
8 F. Wang and X. Liu, *J. Am. Chem. Soc.*, 2008, **130**, 5642-5643.
9 W. Liu, Q. Lin, H. Li, K. Wu, I. Robel, J. M. Pietryga and V. I. Klimov, *J. Am. Chem. Soc.*, 2016, **138**, 14954-14961.
10 Z. Ma, Z. Liu, S. Lu, L. Wang, X. Feng, D. Yang, K. Wang, G. Xiao, L. Zhang, S. A. T. Redfern and B. Zou, *Nat. Commun.*, 2018, **9**, 4506.
11 V. A. Vlaskin, N. Janssen, J. van Rijssel, R. Beaulac and D. R. Gamelin, *Nano Lett.*, 2010, **10**, 3670-3674.
12 Y. Pan, X. Xie, Q. Huang, C. Gao, Y. Wang, L. Wang, B. Yang, H. Su, L. Huang and W. Huang, *Adv. Mater.*, 2018, **30**, 1705256.
13 C. Zhang, L. Yang, J. Zhao, B. Liu, M.-Y. Han and Z. Zhang, *Angew. Chem. Int. Ed.*, 2015, **54**, 11531-11535.
14 O. Chen, D. E. Shelby, Y. Yang, J. Zhuang, T. Wang, C. Niu, N. Omenetto and Y. C. Cao, *Angew. Chem. Int. Ed.*, 2010, **49**, 10132-10135.
15 R. Zhang, X. Mao, Y. Yang, S. Yang, W. Zhao, T. Wumaier, D. Wei, W. Deng and K. Han, *Angew. Chem. Int. Ed.*, 2019, **58**, 2725-2729.
16 Z. Gan, H. Xu and Y. Hao, *Nanoscale*, 2016, **8**, 7794-7807.
17 K. Jiang, L. Zhang, J. Lu, C. Xu, C. Cai and H. Lin, *Angew. Chem. Int. Ed.*, 2016, **55**, 7231-7235.
18 S. Yang, D. Wu, W. Gong, Q. Huang, H. Zhen, Q. Ling and Z. Lin, *Chem. Sci.*, 2018, **9**, 8975-8981.
19 M. Ding, B. Dong, Y. Lu, X. Yang, Y. Yuan, W. Bai, S. Wu, Z. Ji, C. Lu, K. Zhang and H. Zeng, *Adv. Mater.*, 2020, **32**, 2002121.
20 A. Abdollahi, H. Roghani-Mamaqani, B. Razavi and M. Salami-Kalajahi, *ACS Nano*, 2020, **14**, 14417-14492.
21 D. Jaque and F. Vetrone, *Nanoscale*, 2012, **4**, 4301-4326.
22 L. Zhou, R. Wang, C. Yao, X. Li, C. Wang, X. Zhang, C. Xu, A. Zeng, D. Zhao and F. Zhang, *Nat. Commun.*, 2015, **6**, 6938.
23 A. M. Chizhik, S. Stein, M. O. Dekaliuk, C. Battle, W. Li, A. Huss, M. Platen, I. A. T. Schaap, I. Gregor, A. P. Demchenko, C. F. Schmidt, J. Enderlein and A. I. Chizhik, *Nano Lett.*, 2016, **16**, 237-242.
24 Y.-P. Sun, B. Zhou, Y. Lin, W. Wang, K. A. S. Fernando, P. Pathak, M. J. Meziani, B. A. Harruff, X. Wang, H. Wang, P. G. Luo, H. Yang, M. E. Kose, B. Chen, L. M. Veca and S.-Y. Xie, *J. Am. Chem. Soc.*, 2006, **128**, 7756-7757.

25 L. Pan, S. Sun, A. Zhang, K. Jiang, L. Zhang, C. Dong, Q. Huang, A. Wu and H. Lin, *Adv. Mater.*, 2015, **27**, 7782-7787.
26 S. K. Cushing, M. Li, F. Huang and N. Wu, *ACS Nano*, 2014, **8**, 1002-1013.
27 Z. Deng, L. Tong, M. Flores, S. Lin, J.-X. Cheng, H. Yan and Y. Liu, *J. Am. Chem. Soc.*, 2011, **133**, 5389-5396.
28 J. Yin, P. Maity, M. D. Bastiani, I. Dursun, O. M. Bakr, J.-L. Brédas and O. F. Mohammed, *Sci. Adv.*, 2017, **3**, e1701793.
29 M. I. Saidaminov, J. Almutlaq, S. Sarmah, I. Dursun, A. A. Zhumekenov, R. Begum, J. Pan, N. Cho, O. F. Mohammed and O. M. Bakr, *ACS Energy Lett.*, 2016, **1**, 840-845.
30 L. Wang, H. Liu, Y. Zhang and O. F. Mohammed, *ACS Energy Lett.*, 2020, **5**, 87-99.
31 X. Li, S. Xu, F. Liu, J. Qu, H. Shao, Z. Wang, Y. Cui, D. Ban and C. Wang, *ACS Appl. Mater. Interfaces.*, 2021, **13**, 31031-31037.
32 C. Zhou, S. Lee, H. Lin, J. Neu, M. Chaaban, L.-J. Xu, A. Arcidiacono, Q. He, M. Worku, L. Ledbetter, X. Lin, J. A. Schlueter, T. Siegrist and B. Ma, *ACS Mater. Lett.*, 2020, **2**, 376-380.
33 Q. Li, B. Xu, Z. Chen, J. Han, L. Tan, Z. Luo, P. Shen and Z. Quan, *Adv. Funct. Mater.*, 2021, **31**, 2104923.
34 M. Li, J. Zhou, G. Zhou, M. S. Molokeev, J. Zhao, V. Morad, M. V. Kovalenko and Z. Xia, *Angew. Chem. Int. Ed.*, 2019, **58**, 18670-18675.
35 M. Lee, D. H. D. Lee, S. V. Hong, H. Y. Woo, J.-Y. Chae, D. W. Lee, M. J. Han and T. Paik, *Adv. Opt. Mater.*, 2022, **10**, 2102727.
36 W. J. Mir, T. Sheikh, H. Arfin, Z. Xia and A. Nag, *NPG Asia Mater.*, 2020, **12**, 9.
37 G. Pan, X. Bai, D. Yang, X. Chen, P. Jing, S. Qu, L. Zhang, D. Zhou, J. Zhu, W. Xu, B. Dong and H. Song, *Nano Lett*, 2017, **17**, 8005-8011.
38 Z. Zeng, Y. Xu, Z. Zhang, Z. Gao, M. Luo, Z. Yin, C. Zhang, J. Xu, B. Huang, F. Luo, Y. Du and C. Yan, *Chem. Soc. Rev.*, 2020, **49**, 1109-1143.
39 K. Binnemans, *Chem. Rev.*, 2009, **109**, 4283-4374.
40 G. Chen, H. Qiu, P. N. Prasad and X. Chen, *Chem. Rev.*, 2014, **114**, 5161-5214.
41 B. Zhou, B. Shi, D. Jin and X. Liu, *Nat. Nanotechnol.*, 2015, **10**, 924-936.
42 F. Auzel, *Chem. Rev.*, 2004, **104**, 139-174.
43 R. Deng, F. Qin, R. Chen, W. Huang, M. Hong and X. Liu, *Nat. Nanotechnol.*, 2015, **10**, 237-242.
44 R. Gao, D. Yan, D. G. Evans and X. Duan, *Nano Res.*, 2017, **10**, 3606-3617.
45 D. Lee, M. Kim, H.-Y. Woo, J. Chae, D. Lee, S. Jeon, S. J. Oh and T. Paik, *RSC Adv.*, 2020, **10**, 7126-7133.
46 H. J. Seifert, *J. Therm. Anal. Calorim.*, 2006, **83**, 479-505.
47 H. J. Seifert, H. Fink and B. Baumgartner, *J. Solid State Chem.*, 1993, **107**, 19-26.
48 J. Huang, T. Lei, M. Siron, Y. Zhang, S. Yu, F. Seeler, A. Dehestani, L. N. Quan, K. Schierle-Arndt and P. Yang, *Nano Lett.*, 2020, **20**, 3734-3739.
49 K. M. Walsh, K. Pressler, M. J. Crane and D. R. Gamelin, *ACS Nano*, 2022, **16**, 2569-2576.
50 Z. Yang, Z. Jiang, X. Liu, X. Zhou, J. Zhang and W. Li, *Adv. Opt. Mater.*, 2019, **7**, 1900108.
51 W. Lv, Y. Jia, Q. Zhao, M. Jiao, B. Shao, W. Lü and H. You, *Adv. Opt. Mater.*, 2013, **2**, 183-188.
52 X. Wang, R. R. Valiev, T. Y. Ohulchanskyy, H. Ågren, C. Yang and G. Chen, *Chem. Soc. Rev.*, 2017, **46**, 4150-4167.
53 J. K. Swabeck, S. Fischer, N. D. Bronstein and A. P. Alivisatos, *J. Am. Chem. Soc.*, 2018, **140**, 9120-9126.
54 H. Bahmani Jalali, A. Pianetti, J. Zito, M. Imran, M. Campolucci, Y. P. Ivanov, F. Locardi, I. Infante, G. Divitini, S. Brovelli, L. Manna and F. Di Stasio, *ACS Energy Lett.*, 2022, **7**, 1850-1858.
55 S. A. Vieira, N. Rakov, C. B. de Araújo and E. L. Falcão-Filho, *Opt. Mater. Express*, 2019, **9**, 3952-3961.
56 O. M. t. Kate, J. R. v. Ommen and H. T. B. Hintzen, *J. Mater. Chem. C*, 2019, **7**, 6289-6300.
57 P. Dorenbos, *J. Phys.: Condens. Matter*, 2006, **17**, 8103-8111.
58 C.-H. Huang, Y.-C. Chiu and W.-R. Liu, *Eur. J. Inorg. Chem.*, 2014, **2014**, 3674-3680.
59 Y. Chen, F. Pan, M. Wang, X. Zhang, J. Wang, M. Wu and C. Wang, *J. Mater. Chem. C*, 2016, **4**, 2367-2373.
60 T. Jun, K. Sim, S. Iimura, M. Sasase, H. Kamioka, J. Kim and H. Hosono, *Adv. Mater.*, 2018, **30**, 1804547.
61 J. Zhong, D. Chen, H. Xu, W. Zhao, J. Sun and Z. Ji, *J. Alloys Compd.*, 2017, **695**, 311-318.
62 W.-T. Chen, H.-S. Sheu, R.-S. Liu and J. P. Attfield, *J. Am. Chem. Soc.*, 2012, **134**, 8022-8025.
63 B. Deng, S. Liu, C.-s. Zhou, H. Liu, J. Chen and R. Yu, *Chem. Eur. J.*, 2018, **24**, 11627-11636.
64 J.-L. Xie, Z.-Q. Huang, B. Wang, W.-J. Chen, W.-X. Lu, X. Liu and J.-L. Song, *Nanoscale*, 2019, **11**, 6719-6726.